

2000

From Crystals to Columnar Liquid Crystal Phases: Molecular Design, Synthesis and Phase Structure Characterization of a Series of Novel Phenazines Potentially Useful in Photovoltaic Applications

Siwei Leng, *University of Akron Main Campus*

Li Hsin Chan

Jiaokai Jing, *University of Akron Main Campus*

Jie Hu, *University of Akron Main Campus*

Rasha M. Moustafa, *American University of Beirut*, et al.



From crystals to columnar liquid crystal phases: molecular design, synthesis and phase structure characterization of a series of novel phenazines potentially useful in photovoltaic applications

Siwei Leng,^a Li Hsin Chan,^b Jiaokai Jing,^a Jie Hu,^a Rasha M. Moustafa,^c Ryan M. Van Horn,^a Matthew J. Graham,^a Bin Sun,^d Meifang Zhu,^d Kwang-Un Jeong,^e Bilal R. Kaafarani,^c Wenbin Zhang,^a Frank W. Harris^a and Stephen Z. D. Cheng^{*a}

Received 26th June 2009, Accepted 23rd September 2009

First published as an Advance Article on the web 2nd November 2009

DOI: 10.1039/b912634a

It is known that in photovoltaic applications, columnar discotic liquid crystal (LC) phases of conjugated compounds are useful to align the molecules for improving their charge mobilities. However, conjugated compounds are usually either crystalline or amorphous. For compounds to form columnar discotic LC phases, specific molecular design is required for their ordered structural packing. In our recent report, a series of conjugated compounds, 6,7,15,16-tetrakis(alkylthio)quinoxalino-[2',3':9,10]-phenanthro[4,5-*abc*]phenazine (TQPP-[SC_n]₄) (*n* = 6, 8, 10 and 12), which display p-channel characteristics, were synthesized and characterized. This series of compounds was crystalline and did not exhibit LC behavior (S. Leng, B. Wex, L. H. Chan, M. J. Graham, S. Jin, A. J. Jing, K.-U. Jeong, R. M. Van Horn, B. Sun, M. Zhu, B. R. Kaafarani and S. Z. D. Cheng, *J. Phys. Chem. B*, 2009, **113**, 5403–5411). In order to create a columnar LC phase with the lowest free energy within a broad applicable temperature region, we specifically designed and synthesized several series of electron-deficient phenazine derivatives to disrupt the molecular crystal packing and force the compounds to enter the columnar LC phase. These phenazine derivatives were designed to control the fused rigid ring size and shape as well as the location, lengths, and chemical structures of their flexible tails. These series include a series of 2,11-bis(1-methylethyl)-6,7,15,16-tetrakis(alkoxy)quinoxalino[2',3':9,10]phenanthro-[4,5-*abc*]-phenazines (TQPP-[*t*-Bu]₂-[OR(B)]₄), a series of 2,13-bis(1-methylethyl)-7,8,18,19-tetrakis(alkoxy)pyrazino[2,3-*i*]pyrazino[2'',3'':6',7']quinoxalino[2',3':9,10]phenanthro[4,5-*abc*]-phenazines (TPPQPP-[*t*-Bu]₂-[OR(B)]₄), and a series of 3,4,11,12,19,20-hexaalkoxy-2,5,7,8,10,13,15,16,18,21,23,24-dodecaazatri-anthracenes (HDATAN-[OR]₆), where R is the alkyl chain in the substituents and B represents that they are branched structures. The different phase structures and transition behaviors of these series of compounds were studied, and based on the experimental results, we can conclude that tailoring the alkyl tail size, the core size, and the core shape leads to a promising way to design molecules that exhibit the columnar LC phase. In particular, changes in alkyl tail architecture affect the phase behaviors more significantly than changes in its length.

Introduction

Organic charge-transporting materials is a field of intense scientific activity because of their potential application in electronic and optoelectronic devices such as field effect transistors (FETs),^{1,2} light emitting diodes (LEDs),^{3,4} and photovoltaic (PV) cells.^{5,6} The interest in organic PVs arises from the fact that they could be the basis for new, portable renewable-energy generation

technology. Photovoltaics using organic materials are attractive due to their potentially low cost, light weight, ability to be manufactured into large-area structures, and chemical flexibility enabling a tunable energy gap. However, organic photovoltaics still cannot compete with inorganics in terms of efficiency and stability. As a result, much effort has been devoted to the development of novel PV materials and structures in order to improve their performance.

In developing novel organic PV materials, liquid crystals (LCs) are currently viewed as highly potential organic semiconductors due to their order and dynamics.⁷ LCs have advantages over amorphous materials at the point of order which is likely the most important parameter that determines the performances of organic semiconductors in devices. They also provide the decisive advantage of controlling order in the bulk and at interfaces when compared with crystalline materials.

Another more striking ability of LCs is the role of dynamics in organic semiconductors, which is less studied. LCs have the

^aInstitute of Polymer Science and Engineering, Department of Polymer Science, The University of Akron, Akron, Ohio, 44325-3909, USA. E-mail: scheng@uakron.edu

^bDepartment of Applied Materials and Optoelectronic Engineering, National Chi Nan University, Nantou Hsien, 54561, Taiwan

^cDepartment of Chemistry, American University of Beirut, Beirut, Lebanon

^dState Key Laboratory for Chemical Fibers and Polymer Materials, College of Materials Science and Engineering, Donghua University, Shanghai, China

^eDepartment of Polymer-Nano Science and Technology, Chonbuk National University, Jeonju, Jeollabuk-do, Korea

ability to “self-heal” structural defects such as grain boundaries due to their liquid-like property. Under simple thermal annealing, they usually can spontaneously form large single domains that extend over several square millimetres for films up to several micrometres thick.^{8,9} The orientation of molecules within these domains can be controlled by various methods, such as a surface alignment layer, a concentration or temperature gradient, polarized light, or an electronic or magnetic field.^{10–13} The two-dimensional (2D) chemical structure of discotic LCs exhibits a set of unique features. Columns of discotic mesogens can provide one-dimensional charge transport with ability to correct the occurrence of defects.^{6,12}

Synthesis of columnar LCs has been driven by the structural diversity needed to establish reliable structure–property relationships. Several molecular concepts need to be investigated. These include: the chemical structure, the symmetry and size of the rigid core, properties of the connecting groups between the conjugated core and the flexible side chains, and phase behaviors and transitions by variations of the rigid core and connected substituents.^{14–21} To investigate the structure–property relationships of columnar LCs, three series of compounds have been synthesized. According to the previous study, the variation of the length of the flexible alkyl chains is not an effective method to obtain LCs.²²

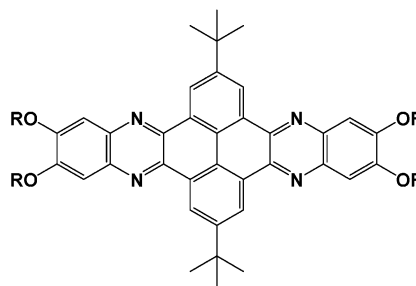
In this study, we modified the architecture of the attached side chains and the length of the rigid core, as well as its symmetry, to obtain LCs at low temperatures that can be easily processed. These compounds were then studied mainly using differential scanning calorimetry (DSC) and wide-angle X-ray diffraction (WAXD). Based on phase transition properties and phase structure identification, it can be concluded that: first, the isotropization temperature decreases as the length of flexible alkyl chain increases; second, a columnar LC phase can be obtained by attaching bulky *tert*-butyl groups; third, branched alkyl side chains are efficient to obtain LCs at room temperature; and finally, changing the volume ratio between rigid core and flexible chains will affect the phase behavior dramatically.

Experimental

Materials and sample preparation

The synthesis of the first series of compounds used in this study, 2,11-bis(1-methylethyl)-6,7,15,16-tetrakis(alkoxy)quinoxalino[2',3':9,10]phenanthro[4,5-*abc*]phenazine, was described in a previous reference.²³ This series of compounds is abbreviated as TQPP-*[t*-Bu]₂-[OR(B)]₄, where R is the alkyl chain in the substituents and B will be used to indicate branched substituents. The molecular structure of these compounds is shown in Scheme 1.

Another series of compounds, 2,13-bis(1-methylethyl)-7,8,18,19-tetrakis(alkoxy)pyrazino[2,3-*i*]pyrazino[2'',3'':6',7']quinoxalino[2',3':9,10]phenanthro[4,5-*abc*]phenazine, were also synthesized.²⁴ They are abbreviated as TPPQPP-*[t*-Bu]₂-[OR(B)]₄, where R and B have the identical meanings as in Scheme 1. This series of compounds shows a similar structure to TQPP-*[t*-Bu]₂-[OR]₄ but has an extended length of the rigid core with one more pyrazine group on each side. The molecular structure of these compounds is shown in Scheme 2.



TQPP-*[t*-Bu]₂-[OR]₄, R = *n*-C_nH_{2n+1}, *n* = 6–14 and 16
TQPP-*[t*-Bu]₂-[ORB]₄, *n* = 20, R =

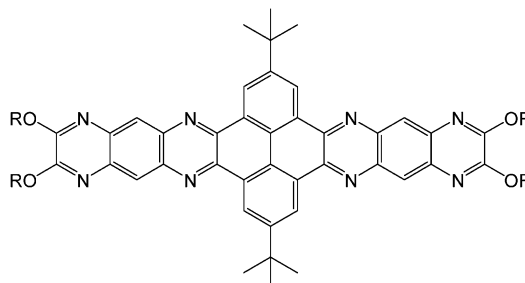
Scheme 1 Chemical structure of TQPP-*[t*-Bu]₂-[OR(B)]₄.

The third series of compounds, 3,4,11,12,19,20-hexaalkoxy-2,5,7,8,10,13,15,16,18,21,23,24-dodecaazatrianthracene, are hexaazatrinaphthylene derivatives with six alkoxy chains of different lengths and were synthesized by treating hexaketocyclohexane octahydrate with the 2,3-dialkoxy-6,7-diaminoquinoxalines in refluxing benzene.²⁴ They are abbreviated as HDATAN-[OR]₆, where R is the alkyl chain in the substituents. The general chemical structure of this series of compounds is shown in Scheme 3.

The samples were vacuum-dried before carrying out the analysis and characterization. For differential scanning calorimetry (DSC) measurements, powder samples were used with a typical weight of 2–3 mg. Melt-cast samples for both wide-angle X-ray diffraction (WAXD) powder (1D) and oriented (2D) experiments were prepared. Their thicknesses were controlled to be around 0.5 mm. The oriented samples were obtained *via* mechanical shearing at a high temperature.

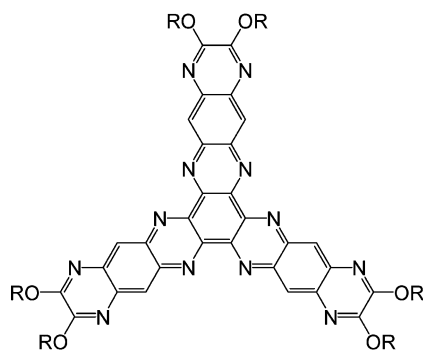
Instruments and experiments

A Perkin-Elmer PYRIS Diamond DSC with an Intracooler 2P apparatus was used to characterize the thermal properties of the phase transitions. For different heating and cooling scanning rates (1–40 °C min^{−1}), the temperature and heat flow scales were calibrated using standard materials. The samples were first heated above their melting temperatures to eliminate thermal history. For each identical cooling and heating scanning rate, the cooling experiments were always carried out first. The transition



TPPQPP-*[t*-Bu]₂-[OR]₄, *n* = 20, R =

Scheme 2 Chemical structure of TPPQPP-*[t*-Bu]₂-[OR(B)]₄.



HDATAN-[OR]₆, $n = 10, 11, 14$ and 15 , $R = n\text{-C}_n\text{H}_{2n+1}$

Scheme 3 Chemical structure of HDATAN-[OR]₆.

temperatures were determined by measuring onset and peak temperatures from the cooling and heating experiments.

1D WAXD experiments were studied with a Rigaku MultiFlex 2 kW tube-anode X-ray (Cu K_α radiation) generator attached to a diffractometer. Phase structure transitions as a function of temperature were obtained with a hot-stage-equipped diffractometer. The hot stage was calibrated with a temperature deviation within $\pm 0.5^\circ\text{C}$. The 1D WAXD patterns were studied across a 2θ range of 1.5 to 40° at a 2°min^{-1} scanning rate. The peak positions were calibrated using silicon powder in the high angle region ($>15^\circ$) and silver behenate in the low-angle region ($<15^\circ$). Background scattering was subtracted from the sample patterns. 2D WAXD patterns were obtained with a Rigaku 18 kW rotating anode X-ray generator coupled to an R-AXIS-IV image plate system. A hot stage, with temperature control to $\pm 0.5^\circ\text{C}$, was also coupled to the diffractometer to obtain images at desired temperatures. To get high quality WAXD patterns, the exposure time was set to 60 min. The same standards were used to calibrate the 2θ angles. The crystal unit cells were determined by constructing reciprocal lattices. Computer refinement was conducted to find the solutions with the least error between the calculated values and the experimental results.^{25–27}

The LC textures were observed using a polarized light microscope (PLM, Olympus BH-2). The experiments were also coupled with a Mettler hot stage (FP-90) for observing phase morphologies at different temperatures.

Results and discussion

Thermodynamic transition properties

Cooling and subsequent heating experiments in DSC were conducted on all series of compounds. Using this technique, the phase transition properties were determined. The relationship between core structure, alkyl chain structure, and alkyl chain length was analyzed over the series of compounds. The simplest structure was for the TQPP-[*t*-Bu]₂-[OR]₄ compounds with linear alkyl chains. The highest transition temperatures of the series of TQPP-[*t*-Bu]₂-[OR]₄ ($R = \text{C}_n\text{H}_{2n+1}$) compounds with $n = 6$ – 8 carbons in the flexible side chains were much higher than 300°C , which enter the degradation limit of the compounds. Only compounds with highest transition temperatures near to or lower than 300°C have been discussed in this study.

Fig. 1 shows a set of DSC cooling and subsequent heating thermo-diagrams for the series of TQPP-[*t*-Bu]₂-[OR]₄ ($R = \text{C}_n\text{H}_{2n+1}$, $n = 9$ – 14 and 16) at a scanning rate of $10^\circ\text{C min}^{-1}$. All of these compounds generally showed more than two phase transitions, and most of these transitions can be observed while heating and cooling, indicating that these thermal transitions are enantiotropic.^{28–30} The highest transition temperatures of these seven compounds measured during heating decreased from 304°C to 191°C , when the number of carbons in their flexible tails changed from 9 to 16. Different cooling and heating rates were used to study the rate dependence of the thermal transition temperatures.

The DSC thermal diagrams of TQPP-[*t*-Bu]₂-[OC₁₀H₂₁]₄ at different cooling and subsequent heating rates (2.5 – $40^\circ\text{C min}^{-1}$) are shown in Fig. 2 as an example. At a $2.5^\circ\text{C min}^{-1}$ cooling rate, the transition temperatures were at 263.3 , 190.3 , and 148.4°C . The corresponding heats of transition were 12.8 , 10.6 , and 19.8 kJ mol^{-1} , respectively. The onset temperatures and heats of transition of the high-temperature transition process are not

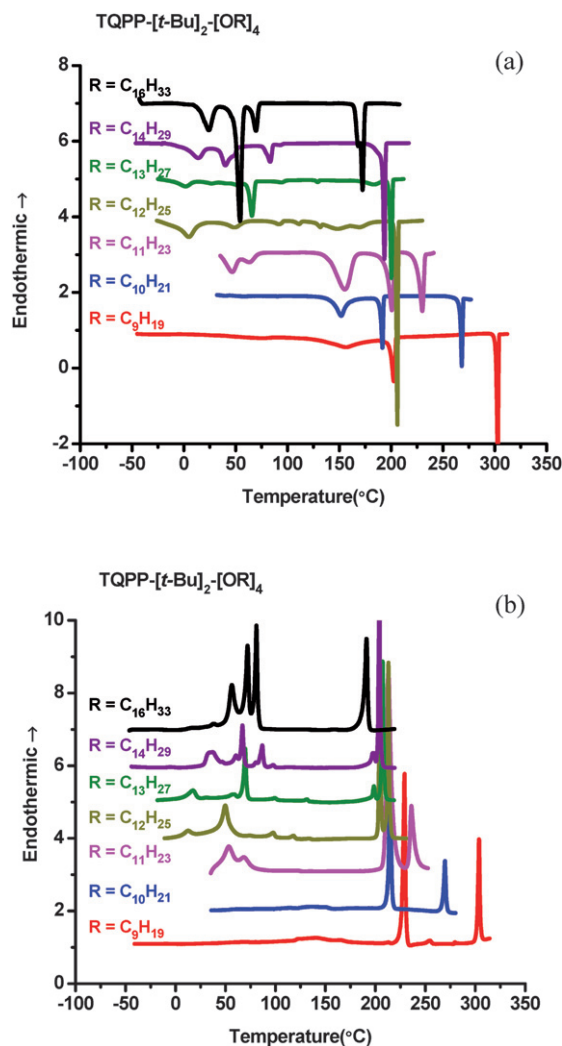


Fig. 1 Sets of DSC cooling and heating diagrams for TQPP-[*t*-Bu]₂-[OR]₄ ($R = \text{C}_n\text{H}_{2n+1}$, $n = 9$ – 14 and 16) samples at a scanning rate of $10^\circ\text{C min}^{-1}$ cooling (a) and heating (b).

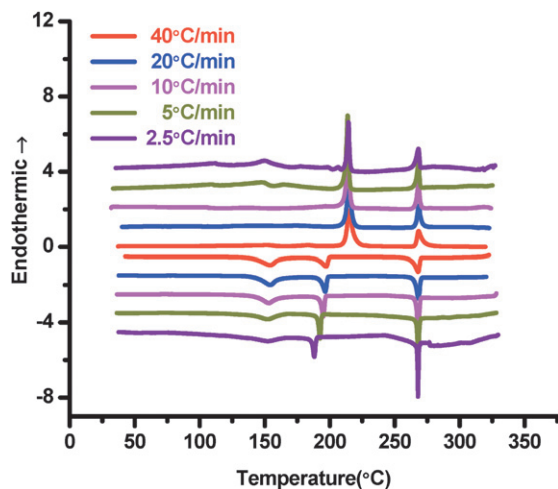


Fig. 2 Thermal diagram of TQPP-[*t*-Bu]₂-[OC₁₀H₂₁]₄ at different cooling and heating rates.

cooling and heating rate dependent, indicating that this transition may be associated with an equilibrium transition of a meso-phase (most likely, it is a discotic LC phase). On the other hand, those of the low-temperature transition processes appear to exhibit cooling and heating rate dependence, indicating that the transitions at low temperatures may represent a transition that increases the structural order.^{31–46}

Fig. 3 shows a set of DSC cooling and subsequent heating diagrams for a compound of TQPP-[*t*-Bu]₂-[OC₂₀H₄₁B]₄ with 20 carbons in the branched tails at different cooling and heating rates (2.5–40 °C min^{−1}). The main difference between this compound and the one found in Fig. 2 was the branching in the alkyl tails. It was found that there are two phase transitions. Both transition temperatures and heats of transition of the high-temperature transition are only slightly cooling and heating rate dependent, while the low-temperature ones show a greater dependence on the rate. Furthermore, the highest transition temperature (152.2 °C) is substantially decreased compared with

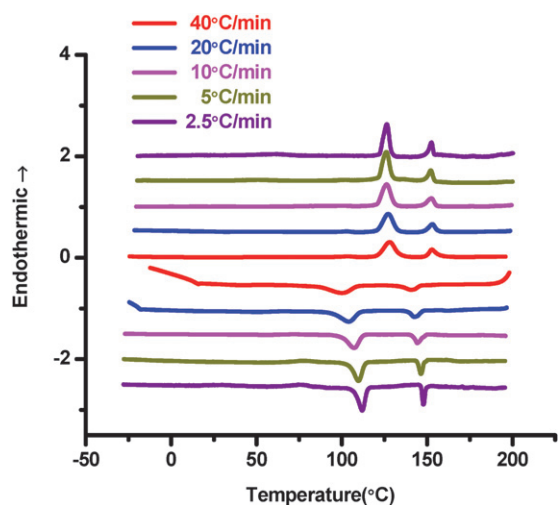


Fig. 3 Thermal diagram of TQPP-[*t*-Bu]₂-[OC₂₀H₄₁B]₄ at different cooling and heating rates.

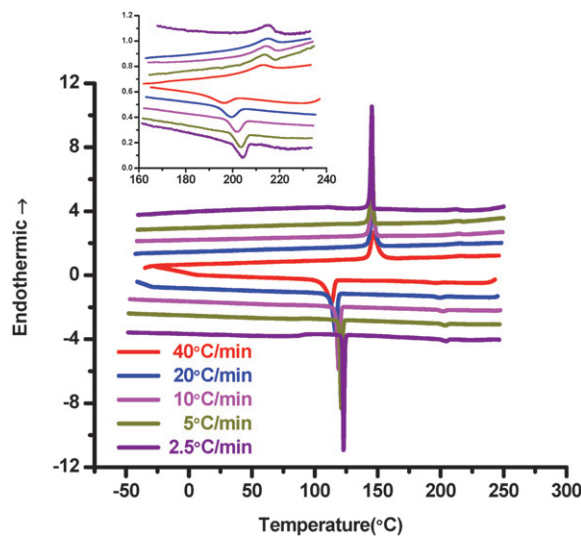


Fig. 4 Thermal diagram of TPPQPP-[*t*-Bu]₂-[OC₂₀H₄₁B]₄ at different cooling and heating rates. The temperature scale from 160 to 240 °C is also shown in the inset for clarity.

that of the linear alkyl tails (note that the tail lengths in this compound are close to that of TQPP-[*t*-Bu]₂-[OC₁₆H₃₃]₄). Based on DSC experiments alone, it may be expected that these two phase transitions must be associated with similar transition behaviors^{31–46} as shown in Fig. 2 for TQPP-[*t*-Bu]₂-[OC₁₀H₂₁]₄.

Fig. 4 is a set of DSC cooling and subsequent heating diagrams for a compound of TPPQPP-[*t*-Bu]₂-[OC₂₀H₄₁B]₄ with identical branched tails to the compound shown in Fig. 3. This compound has two more rigid rings in the core of the compound (Scheme 2) compared with TQPP-[*t*-Bu]₂-[OC₂₀H₄₁B]₄. It is evident that a high-temperature transition occurs at 215.0 °C with a weak enthalpic contribution of 0.9 kJ mol^{−1} (shown in the inset). This transition was only slightly cooling and heating rate dependent. A low-temperature transition takes place around 145.1 °C with a significant contribution from the enthalpy change (33.6 kJ mol^{−1} at 2.5 °C min^{−1} heating rate), and this transition is cooling and

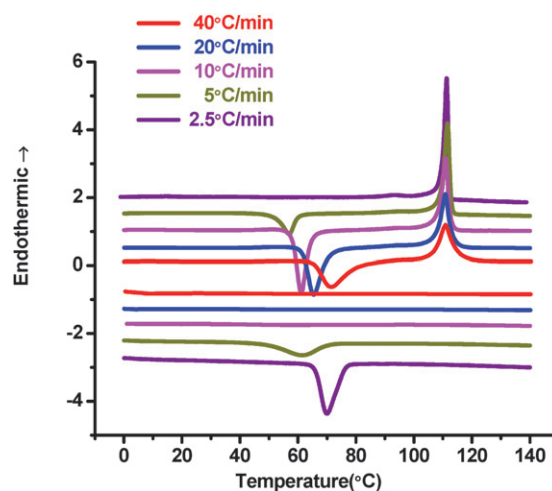


Fig. 5 Thermal diagram of HDATAN-[OC₁₄H₂₉]₆ at different cooling and heating rates.

heating rate dependent in both transition temperature and heat of transition. Compared with Fig. 3, an increase in the rigid core length leads to a substantial increase in the highest transition temperature, yet a mesophase can apparently still be found around 215 °C.

For the series of compounds with a non-linear core, HDA-TAN-[OR]₆, Fig. 5 shows a set of DSC experiments of HDA-TAN-[OC₁₄H₂₉]₆ as an example. It was found that the transition temperatures and heats of transition shown in this figure are dependent on cooling and heating rates. At a cooling rate of 2.5 °C min⁻¹, an exothermic peak is observed. The onset temperature for the transition is at 78.1 °C. When the cooling rate is faster than 10 °C min⁻¹, no exothermic peak can be found, indicating that the rate of this phase formation is relatively slow. At a heating rate of 2.5 °C min⁻¹, the transition temperature is at 111.3 °C, and the heat of transition is 62.6 kJ mol⁻¹. Compared with the DSC cooling diagrams for 2.5 °C min⁻¹ cooling and subsequent heating, a large supercooling is required for the phase formation ($\Delta T = 111.3\text{ }^{\circ}\text{C} - 78.1\text{ }^{\circ}\text{C} = 33.2\text{ }^{\circ}\text{C}$). With increasing cooling and heating rates, an exothermic peak can be observed between 60 and 80 °C, depending upon the heating rates. The endothermic peak observed at a heating rate faster than 2.5 °C min⁻¹ decreases its enthalpy change, indicating that the materials cannot be completely transformed to the ordered structure, although the melting temperature remains constant. All these observations tend to be an indication of crystallization during cooling and crystal melting during heating in this temperature region.

Temperature dependence of phase structure evolution

1D WAXD heating and cooling experiments were conducted to determine the structural transformations in these compounds. Fig. 6 exhibits a set of 1D WAXD patterns of TQPP-[*t*-Bu]₂-[OC₁₀H₂₁]₄ at a cooling rate of 2.5 °C min⁻¹ as an example for this set of compounds. The 1D WAXD patterns were recorded from 290 to 40 °C at an interval of 10 °C. This figure clearly shows that there were four different phases in this temperature region and that the transition temperatures were consistent with those observed in DSC experiments (Fig. 1 and 2). The diffraction peak at 38.13° belongs to aluminium which has been used as a standard substrate in this study. In this figure, structures with two different length scales can be identified. One structure is on the nanometre scale between 1.5° and 9°, and the other is on the sub-nanometre scale between 10° and 35°.

The highest temperature phase, above 270 °C, is the isotropic phase. Only two amorphous halos were observed, which are centered at $2\theta = 17.5^{\circ}$ and 23.0° (*d*-spacings of 0.51 and 0.39 nm, respectively). The amorphous halo at $2\theta = 23.0^{\circ}$ may be attributed to the scattering from the average distance among the alkyl tails, while the amorphous halo at $2\theta = 17.5^{\circ}$ is expected to be caused by the rigid cores. In between 270 and 190 °C, only diffractions in the low-angle region of the 1D WAXD patterns were observed at $2\theta = 3.05^{\circ}$, 5.95° , 7.37° , 11.54° , and 11.95° (corresponding to *d*-spacings of 2.89, 1.49, 1.20, 0.77, and 0.74 nm, respectively), which are shown in the inset of Fig. 6. No diffraction in the high angle region ($>15^{\circ}$) was found, indicating that no long-range order exists in the molecular packing from the low-angle region of WAXD. This set of results reveals that

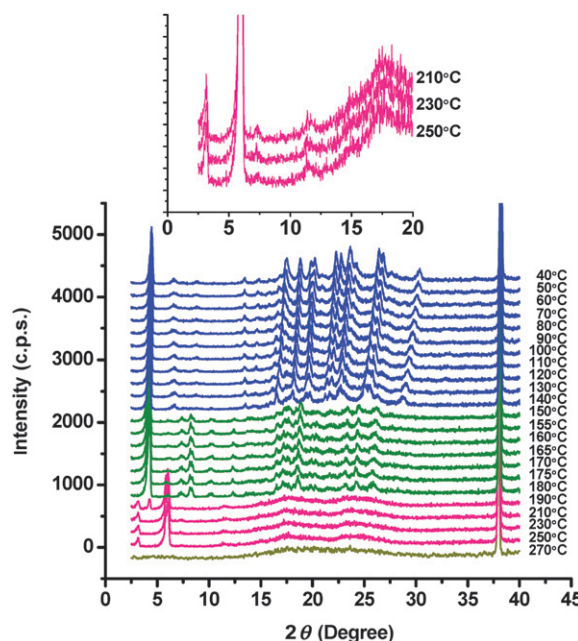


Fig. 6 1D WAXD patterns of TQPP-[*t*-Bu]₂-[OC₁₀H₂₁]₄ while cooling at 2.5 °C min⁻¹ and the diffraction patterns at 250 °C, 230 °C, and 210 °C are shown in the inset for clarity.

TQPP-[*t*-Bu]₂-[OC₁₀H₂₁]₄ may possess an LC phase within which the columns are packed in a 2D rectangular lattice (see below for detailed structure assignment).

This conclusion is supported by PLM observations of the phase textures. TQPP-[*t*-Bu]₂-[OC₁₀H₂₁]₄ exhibited a fan-like texture at 220 °C (below the isotropization temperature of 270 °C) as shown in Fig. 7a, which is often observed in columnar LC phases.^{47,48} Further cooling to a temperature region below 190 °C, the phase texture of TQPP-[*t*-Bu]₂-[OC₁₀H₂₁]₄ changed suddenly to a crystalline morphology (Fig. 7b). A further decrease to room temperature did not alter the crystalline morphology, but changed the birefringence slightly (Fig. 7c). These texture changes correspond closely to the appearance of the sharp diffraction peaks at both high and low 2θ angles as shown in Fig. 6, indicating that the first, higher temperature transition at 190.3 °C is associated with the columnar LC-to-crystalline phase transition, while the lower temperature transition at 148.4 °C from DSC and WAXD is a crystal-to-crystal transition. Note from our previous work that there was no LC phase formed in the case of TQPP-[SC₁₀]₄, which has similar side chains to TQPP-[*t*-Bu]₂-[OC₁₀H₂₁]₄ but has no substituents at the 2 and 11 positions.²² The formation of the LC phase in TQPP-[*t*-Bu]₂-[OC₁₀H₂₁]₄ indicates that the introduction of bulky *tert*-butyl groups at the 2 and 11 positions plays a key role in forming a mesophase.

The effect of flexible tails on the phase behavior was examined by modifying the flexible linear alkyl chains to branched alkyl chains, as in the case of TQPP-[*t*-Bu]₂-[OC₂₀H₄₁B]₄ with 20 carbons in the branched tails. Fig. 8 is a set of 1D WAXD patterns for this compound in a temperature region between 160 and 30 °C at 2.5 °C min⁻¹ cooling. It is evident that there existed three phases with two transition temperatures occurring at 148.0 °C and 112.2 °C, corresponding closely to the DSC

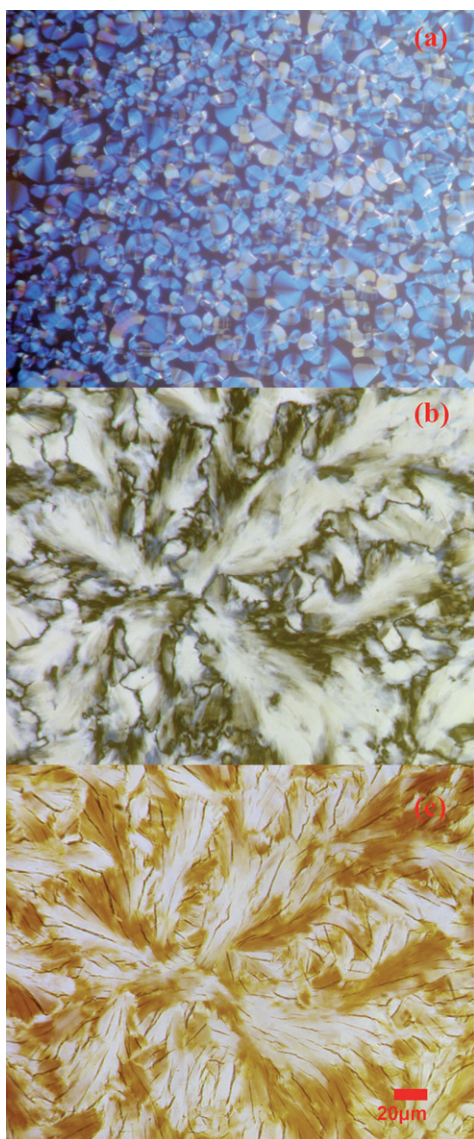


Fig. 7 PLM textures of TQPP-[*t*-Bu]₂-[OC₁₁H₂₃]₄ at 220 °C (a), 170 °C (b), and 30 °C (c).

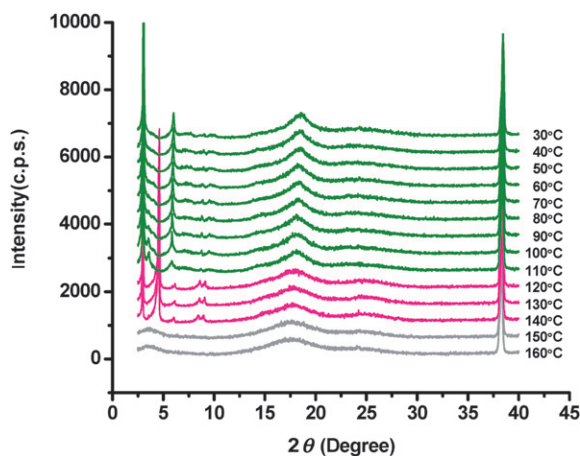


Fig. 8 1D WAXD patterns of TQPP-[*t*-Bu]₂-[OC₂₀H₄₁B]₄ while cooling at 2.5 °C min⁻¹.

results as shown in Fig. 3. Above 148.0 °C, the sample was in an isotropic liquid phase. Below that temperature, sharp diffractions appeared in the low-angle region ($2\theta < 10^\circ$), and only two broad peaks were found around $2\theta = 18.0^\circ$ and 24.7° (corresponding to d -spacings of 0.49 and 0.36 nm, respectively). These structural features most likely indicate two high-order mesophases.

The PLM observations of this compound support these assignments. Fig. 9 shows the phase textures at these two temperatures for TQPP-[*t*-Bu]₂-[OC₂₀H₄₁B]₄. Both morphologies exhibited fan-like textures at 130 °C (Fig. 9a) and 30 °C (Fig. 9b). These are typical columnar liquid crystalline textures.^{40,41} Therefore, we can conclude that non-crystalline flexible tails combined with bulky *tert*-butyl groups near the center can completely eliminate the formation of the crystalline phase.

Fig. 10 shows a set of 1D WAXD patterns recorded at a cooling rate of 2.5 °C min⁻¹ for the compound with the same branched alkyl tails but two more rigid rings in the core, TPPQPP-[*t*-Bu]₂-[OC₂₀H₄₁B]₄. It is observed that above 204 °C, only three amorphous halos were found in both low and high 2θ -angle regions, indicating the isotropic liquid phase. Between 204 °C and 123 °C, only diffractions at low 2θ angles of 2.76° , 4.45° , 5.91° , 8.46° , and 8.90° (corresponding to d -spacings of 3.23, 1.99, 1.50, 1.04, and 0.99 nm, respectively) have been detected. This result reveals that it is a mesophase with a 2D rectangular lattice (see below for detailed structure assignment). Below 123 °C, diffraction peaks at high 2θ angles appeared, indicating the formation of structural order on the molecular level; however, the low-angle diffraction peaks suddenly changed their 2θ -angle positions. This shows that the supramolecular

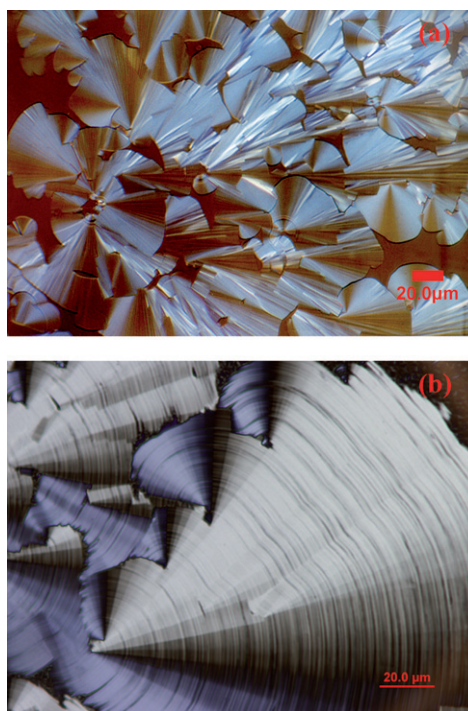


Fig. 9 Liquid crystalline textures of TQPP-[*t*-Bu]₂-[OC₂₀H₄₁B]₄ at 130 °C (a) and 30 °C (b).

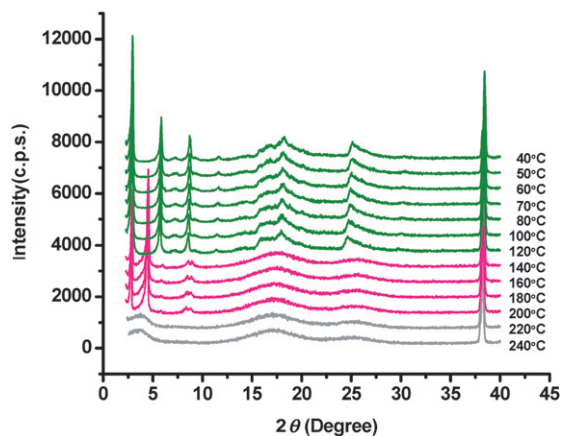


Fig. 10 1D WAXD patterns of TPPQPP-[*t*-Bu]₂-[OC₂₀H₄₁B]₄ while cooling at 2.5 °C min⁻¹.

packing in this low-temperature phase has also changed compared with that of the high-temperature phase.

The PLM phase morphologies for this compound also exhibited columnar LC textures at 190 °C in the high-temperature phase between 204 °C and 123 °C (Fig. 11a).^{47,48} Interestingly enough, even in the low-temperature phase at 30 °C, as shown in Fig. 11b, the major texture has not changed, although at the low-temperature of 30 °C, a more ordered phase has been introduced (Fig. 10). At this temperature, only some cracks are formed due presumably to shrinking of the layer spacing along the columnar axis direction.

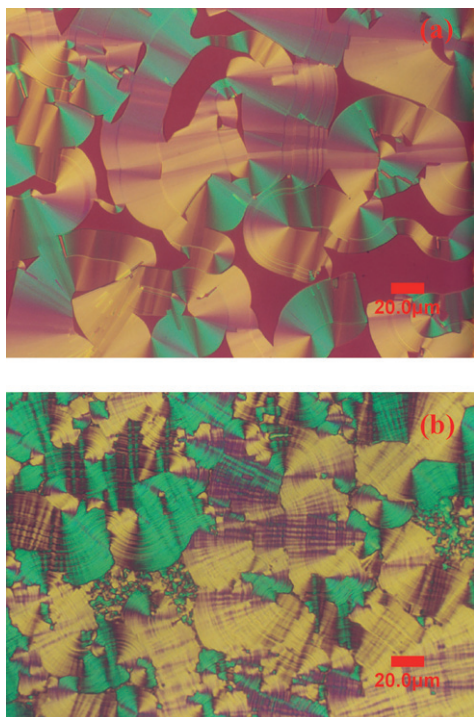


Fig. 11 PLM photographs of TPPQPP-[*t*-Bu]₂-[OC₂₀H₄₁B]₄ at 190 °C (a) and 30 °C (b). In order to enhance the texture visualization, a 530 nm tint plate was inserted.

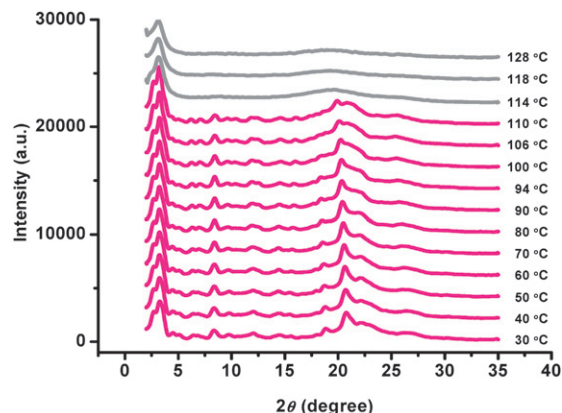


Fig. 12 1D WAXD patterns of HDATAN-[OC₁₄H₂₉]₆ during heating at 2.5 °C min⁻¹.

Fig. 12 is a set of 1D WAXD patterns for HDATAN-[OC₁₄H₂₉]₆ during subsequent heating after cooling at 2.5 °C min⁻¹. Analysis was done during heating because of the phase behavior found in the DSC experiments (shown in Fig. 5). Above 110 °C, two amorphous halos indicative of an isotropic phase were seen at $2\theta = 3.2^\circ$ and 19.0° (corresponding to *d*-spacings of 2.76 and 0.47 nm). They may be related to the radius of the molecule and the average distance among the alkyl tails. When the temperature reached 110 °C, HDATAN-[OC₁₄H₂₉]₆ exhibited a new diffraction pattern. Fig. 12 exhibits partially overlapped diffractions in the low-angle region. In addition, various diffractions can also be observed in the high angle region, indicating a transformation of this compound into the crystalline phase.

Using 1D WAXD experimental results we clearly identified evolution of the phase transitions corresponding to those observed in the DSC experiments. However, precise determinations of these phase structures are necessary to further pursue our discussion of the effects of chemical modifications of rigid cores to generate columnar LC phases. The conclusions of these discussions will serve as principles for the further design of molecular compounds for photovoltaic applications.

Identification of the liquid crystalline and crystalline phase structures

Without structural modifications of the substituents, only crystalline phases were observed in TQPP-[SC_{*n*}]₄, and no LC or any other mesophases existed in this series of compounds.²² With modification of the rigid core by introducing *tert*-butyl-substitutions at the 2 and 11 positions, however, the 1D WAXD results, as shown in Fig. 8 and 10, indicate the generation of mesophases; therefore, we need to identify the crystal and mesophase structures of TQPP-[*t*-Bu]₂-[OR]₄ using 2D WAXD. We use TQPP-[*t*-Bu]₂-[OC₁₀H₂₁]₄ as an example. Based on the shape of the molecule, we speculate that the crystal unit cell dimensions should be very anisotropic, as shown in our previous work for TQPP-[SC_{*n*}]₄.²²

Fig. 13a shows a 2D WAXD pattern for this compound at room temperature after the sample was mechanically sheared at 220 °C. The ring at $2\theta = 28.47^\circ$ belongs to silicon powder which

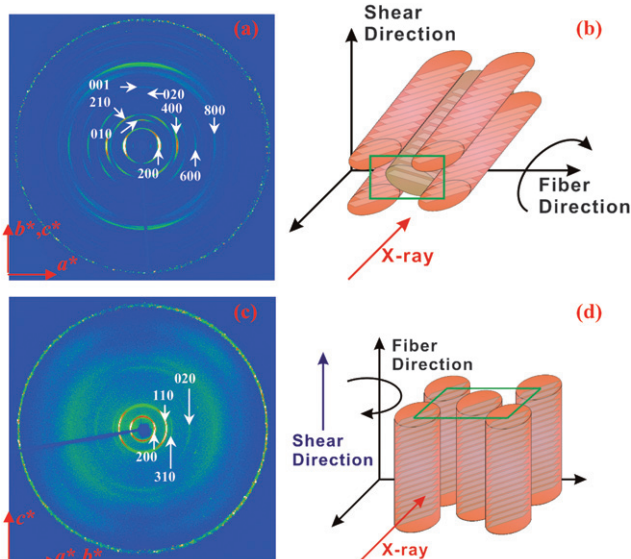


Fig. 13 2D WAXD pattern of TQPP- $[t\text{-Bu}]_2[\text{OC}_{10}\text{H}_{21}]_4$ at room temperature (a) and at 235 °C (c) after the sample was mechanically sheared at 220 °C. The shear and X-ray beam direction as well as the molecular packing are also shown in (b) and (d). For clarity, only the cores of the molecules are shown.

was used as a standard in the 2D WAXD experiments. The 2D WAXD pattern shows clearly that TQPP- $[t\text{-Bu}]_2[\text{OC}_{10}\text{H}_{21}]_4$ was crystalline at room temperature. Along the equator, up to four diffractions can be detected. The d -spacing ratio of these diffractions is 2 : 4 : 6 : 8 (the d -spacing of the first diffraction is actually second order due to the extinction rule, and it is 2.04 nm). Therefore, we assign these diffractions to the a^* -axis along the equator, and they are (200), (400), (600) and (800),

Table 1 Crystallographic parameters of the crystalline phase at room temperature in TQPP- $[t\text{-Bu}]_2[\text{OC}_{10}\text{H}_{21}]_4$

(hkl) plane	$2\theta/\text{deg}$		$d\text{-Spacing}/\text{nm}$	
	Expt. ^a	Calcd. ^b	Expt. ^a	Calcd. ^b
200	4.3	4.3	2.04	2.04
010	6.4	6.4	1.39	1.39
210	7.7	7.7	1.15	1.15
400	8.7	8.7	1.02	1.02
410	10.8	10.8	0.82	0.82
020	12.7	12.7	0.70	0.70
600	13.0	13.0	0.68	0.68
001	14.3	14.2	0.62	0.62
610	14.4	14.5	0.62	0.61
420	15.5	15.4	0.57	0.57
111	15.8	15.7	0.56	0.56
411	17.8	17.9	0.51	0.50
620	18.2	18.3	0.49	0.49
030	19.2	19.2	0.46	0.46
230	19.6	19.6	0.45	0.45
430	21.0	21.1	0.43	0.42
131	24.0	24.0	0.37	0.37
431	25.4	25.5	0.35	0.35

^a Experimentally observed in Fig. 13a. ^b Calculated based on the orthorhombic unit cell of $a = 4.08$ nm, $b = 1.39$ nm, $c = 0.62$ nm, $\alpha = \beta = \gamma = 90^\circ$.

respectively. The long axis of the rigid core of these molecules must be aligned along the a^* -axis as shown in Fig. 13b. The first three diffractions along the meridian are identified as (010), (020), and (001). This was identified as a uniaxial fiber pattern with the rotating axis being the a^* -axis. The b^* and c^* axes were thus along the meridian, which is aligned with the shear direction.

The diffractions in the quadrants indicate that the structure possesses a 3D order. The first diffraction in the quadrant was assigned as the (210) diffraction. Following the standard procedure of determining the structural lattice, a triangle of the (hkl) diffractions can be constructed based on the diffractions of the (200), (010), and (210) planes.^{22,25–27} The unit cell of this phase was determined to be orthorhombic with dimensions of $a = 4.08$ nm, $b = 1.39$ nm, $c = 0.62$ nm, and $\alpha = \gamma = \beta = 90^\circ$ via the refinement of the reciprocal lattice. The discs are tilted with respect to the normal direction of the columns, and the π – π interaction direction has deviated from the normal direction of the columns, resulting in the c -axis dimension being larger than 0.35 nm, which is the typical π – π stacking length. The crystallographic density was calculated to be 1.08 g cm^{−3} with two molecules in each unit cell. The experimental and calculated diffraction angles (2θ) and d -spacing values are listed in Table 1.

Fig. 13c is a 2D WAXD pattern taken at a temperature of 235 °C which is located within the mesophase region of TQPP- $[t\text{-Bu}]_2[\text{OC}_{10}\text{H}_{21}]_4$. According to the reciprocal lattice principle, the (00 l) diffractions are along the meridian (along the sheared direction) and the $(hk0)$ diffractions are along the equator (as illustrated by the sample geometry in this figure). Following the standard procedure of determining the structural lattice, a triangle of the (hkl) diffractions along the equator direction can be constructed. This indicates that there is a layer structure perpendicular to the sheared direction, and a 2D lattice was formed within the layer. The diffractions on the equator correspond to the (200), (110), (310), (020), and (220) diffractions. There were no sharp diffractions in the quadrants. The diffuse diffraction on the meridian corresponds to a layered structure with a d -spacing of 0.63 nm. Again, these molecules are tilted, and the π – π interaction direction has deviated from the normal direction of the columns. It is evident that this is a columnar LC phase since the diffractions on the equator show long-range positional order.

Columnar LC phases have been identified as hexagonal, rectangular, and oblique phases.^{28,49,50} The columnar rectangular LC phases can be specified by three different planar space groups, $P2_1/a$, $P2/a$ and $C2/m$, based on the symmetries of the 2D lattices.

Table 2 Diffraction conditions of the three space groups of columnar rectangular liquid crystalline phases

Space group	Index	Diffraction conditions
$P2_1/a$	hk	—
	$h0$	$h = 2n$
	$0k$	$k = 2n$
$P2/a$	hk	—
	$0k$	$k = 2n$
$C2/m$	hk	$h + k = 2n$
	$h0$	$h = 2n$
	$0k$	$k = 2n$

The molecules are elliptically projected on the plane of the 2D lattices in columnar rectangular LC phases.^{46,51–58} The reflection conditions of these three space groups are listed in Table 2.⁵⁹ According to the indexed diffractions, the high-temperature phase of TQPP- $[t\text{-Bu}]_2\text{-[OC}_{10}\text{H}_{21}]_4$ must be a typical high-order rectangular columnar LC phase (Col_r). This Col_r mesophase shows $C2/m$ symmetry with in-plane dimensions of $a = 5.79$ and $b = 1.53$ nm. Note that this structural orientation is different from that of those reciprocal axes in the crystal phase as described in Fig. 13a. In the crystal phase, only the a^* -axis is along the equator, and the b^* and c^* axes are along the meridian. This indicates that in this mesophase, the molecules form uniaxial columns, yet orientation of the long axis of the molecules has not changed. The mesophase exhibited the ability of “self-healing” the crystal grain defects and formed large domains of uniaxial columns along the shear direction by setting the molecules flat-on and generating π - π interactions among the flat faces of the molecules to construct the Col_r phase. A schematic illustration of the molecular packing is included as Fig. 13d (compared to the randomly oriented columns in a plane in Fig. 13b).

Second, we are particularly interested in TQPP- $[t\text{-Bu}]_2\text{-[OC}_{20}\text{H}_{41}\text{B}]_4$ since it possesses two mesophases in the high- and low-temperature regions. Fig. 14a shows 2D WAXD uniaxial patterns from oriented TQPP- $[t\text{-Bu}]_2\text{-[OC}_{20}\text{H}_{41}\text{B}]_4$ at room temperature, namely, in the high-order mesophase after mechanical shearing at 95 °C. Up to six diffractions have been observed along the equator, and the d -spacing ratio between them is 2 : 4 : 6 : 8 : 10, ..., n . The d -spacing of the first diffraction (second order, again based on the extinction rule) is 3.23 nm. The diffractions along the equator were indexed as (200), (400), (600), (800), (1000), ..., ($h00$), respectively. Following the identical procedure as described in the case of TQPP- $[t\text{-Bu}]_2\text{-[OC}_{10}\text{H}_{21}]_4$,

the first two diffractions on the meridian were then indexed as the (010) and (001) diffractions. However, in this case, there were no diffractions in the quadrants, indicating that only a 2D ordered structure exists. The 2D lattice dimensions were determined to be $a = 6.47$ nm and $b = 1.41$ nm. The angle between the a - and b -axis is 90°. The a^* -axis is along the equator, and it serves as the fiber axis. The b^* and c^* axes are along the meridian. The d -spacing between discs within columns is 0.62 nm with the deviated π - π interaction direction. Compared with the 2D WAXD results shown in Fig. 13a, we can conclude that the flexible tails in TQPP- $[t\text{-Bu}]_2\text{-[OR}]_4$ facilitate the crystalline phases since with non-crystalline branched flexible tails, only high-ordered LC phases can be formed as shown in Fig. 14a. The molecular packing is schematically drawn in Fig. 14b.

When the temperature is above 127 °C, TQPP- $[t\text{-Bu}]_2\text{-[OC}_{20}\text{H}_{41}\text{B}]_4$ enters another high-order mesophase. Fig. 14c shows a 2D WAXD pattern of this compound at 140 °C after the sample was mechanically sheared. The scatter along the meridian and within the quadrants was more diffuse compared with the low-temperature phase. It is evident that this high-temperature mesophase showed less molecular positional order. Along the equator, the diffractions were indexed as (200), (110), (400), (020), and (220). The diffraction of (001) is located on the meridian. The a^* and b^* axes are along the equator, and the c^* -axis (column direction) is along the meridian. The mesophase at 140 °C is also the Col_r phase with $C2/m$ symmetry and an in-plane dimension of $a = 6.10$ and $b = 2.08$ nm. The column axis is perpendicular to the ab -plane, and the molecules are stacked in the column with a d -spacing of 0.59 nm as shown in Fig. 14d.

After extending the rigid core of TQPP- $[t\text{-Bu}]_2\text{-[OC}_{20}\text{H}_{41}\text{B}]_4$ to TPPQPP- $[t\text{-Bu}]_2\text{-[OC}_{20}\text{H}_{41}\text{B}]_4$, two phase transitions can be

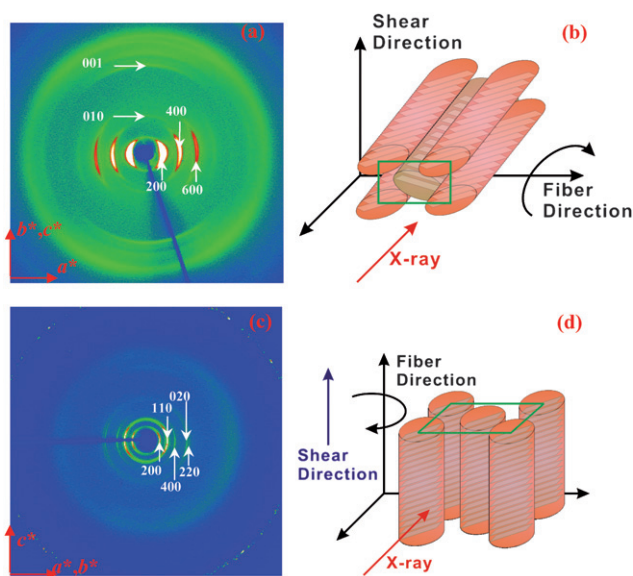


Fig. 14 2D WAXD pattern of TQPP- $[t\text{-Bu}]_2\text{-[OC}_{20}\text{H}_{41}\text{B}]_4$ at room temperature (a) and at 140 °C (c) after the sample was mechanically sheared at 95 °C. The shear and X-ray beam direction as well as the molecular packing are also shown in (b) and (d). For clarity, only the cores of the molecules are shown.

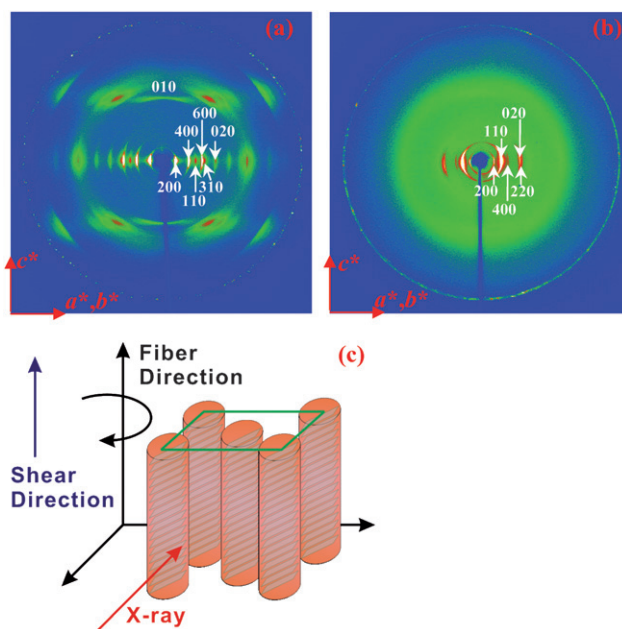


Fig. 15 2D WAXD pattern of TPPQPP- $[t\text{-Bu}]_2\text{-[OC}_{20}\text{H}_{41}\text{B}]_4$ at room temperature (a) and 160 °C (b) after the sample was mechanically sheared at 125 °C. The shear and X-ray beam direction as well as the molecular packing are also shown in (c). For clarity, only the cores of the molecules are shown.

identified based on the DSC and 1D WAXD patterns as shown in Fig. 4 and 10. It can also be seen that the transition temperatures shift to higher values. Furthermore, the low-temperature phase exhibits a more ordered structure compared with that of TPPP-[*t*-Bu]₂-[OC₂₀H₄₁B]₄. Fig. 15a shows a 2D WAXD pattern for TPPQPP-[*t*-Bu]₂-[OC₂₀H₄₁B]₄ taken at room temperature after mechanical shearing at 125 °C. The diffractions along the equator have been indexed as the (200), (400), (110), (600), (310), (020), and (800) diffractions. Therefore, the *a** and *b** axes are on the equator, and the *c**-axis is along the meridian. This is different from the previous two cases. This may reflect that the different lengths of the rigid cores may respond differently to the mechanical shearing process. Although the diffraction arcs off the equator are diffuse, the indices of (*hkl*) in the quadrants as shown in this figure indicate that this phase possesses a 3D ordered structure with small crystal sizes. The indices of (*hkl*) should correspond to crystals from the rigid cores surrounded by the mostly amorphous tails. This may reveal a structure that is crystalline within each of the columns with a lack of long-range order between the side chains. Namely, it is a high-order columnar phase. If this is the case, this phase may be helpful for an effective improvement in the charge mobility along the column direction. A detailed study is underway along this direction.

Following the identical procedure adopted in determining the previous two series of crystal structures in the cases of linear and branched TPPP-[*t*-Bu]₂-[OR]₄, we can determine that *a* = 6.65 nm and *b* = 1.48 nm for TPPQPP-[*t*-Bu]₂-[OC₂₀H₄₁B]₄. The angle between the *a*- and *b*-axis is 114.8°. The layer dimension along the column direction is *c* = 0.64 nm, and the *c*-axis is perpendicular to the *ab*-plane. This indicates that it is a monoclinic unit cell. The crystallographic density was calculated to be 1.05 g cm⁻³ with two molecules in each unit cell. The experimental and calculated diffraction angles (2θ) and *d*-spacing

Table 3 Crystallographic parameters of the crystalline phase at room temperature in TPPQPP-[*t*-Bu]₂-[OC₂₀H₄₁B]₄

<i>(hkl)</i> plane	2θ/deg		<i>d</i> -Spacing/nm	
	Expt. ^a	Calcd. ^b	Expt. ^a	Calcd. ^b
200	2.93	2.93	3.02	3.02
400	5.84	5.85	1.51	1.51
110	7.30	7.30	1.21	1.21
600	8.78	8.79	1.01	1.01
310	9.30	9.31	0.95	0.95
800	11.70	11.72	0.75	0.75
020	13.14	13.14	0.67	0.67
1000	14.66	14.67	0.60	0.60
211	16.10	16.10	0.55	0.55
601	16.39	16.40	0.54	0.54
420	16.50	16.51	0.54	0.54
411	17.35	17.37	0.51	0.51
530	17.93	17.95	0.49	0.49
330	18.32	18.35	0.48	0.48
620	18.67	18.67	0.48	0.48
221	20.18	20.17	0.44	0.44
231	25.35	25.38	0.35	0.35
331	26.09	26.08	0.34	0.34

^a Experimentally observed in Fig. 15a. ^b Calculated based on the monoclinic unit cell of *a* = 6.65 nm, *b* = 1.48 nm, *c* = 0.64 nm, α = β = 90°, γ = 114.8°.

values are listed in Table 3. Note that when the rigid core increases from TPPP-[*t*-Bu]₂-[OC₂₀H₄₁B]₄ to TPPQPP-[*t*-Bu]₂-[OC₂₀H₄₁B]₄, the *a*-axis, *b*-axis, and *c*-axis have slightly increased. These results thus reflect how the molecules pack into the lattice. The long axis of the rigid core must be aligned along the *a*-axis, while the *c*-axis represents the core stacking direction.

Fig. 15b shows a 2D WAXD pattern for the TPPQPP-[*t*-Bu]₂-[OC₂₀H₄₁B]₄ taken at 160 °C after mechanical shearing. No diffractions in the quadrants were found, indicating that only a mesophase existed. The diffractions on the equator were identified as the (200), (110), (310), (020), and (220) diffractions. The *a** and *b** axes are thus along the equator. The diffraction on the meridian was indexed as (001), and therefore, the *c**-axis is on

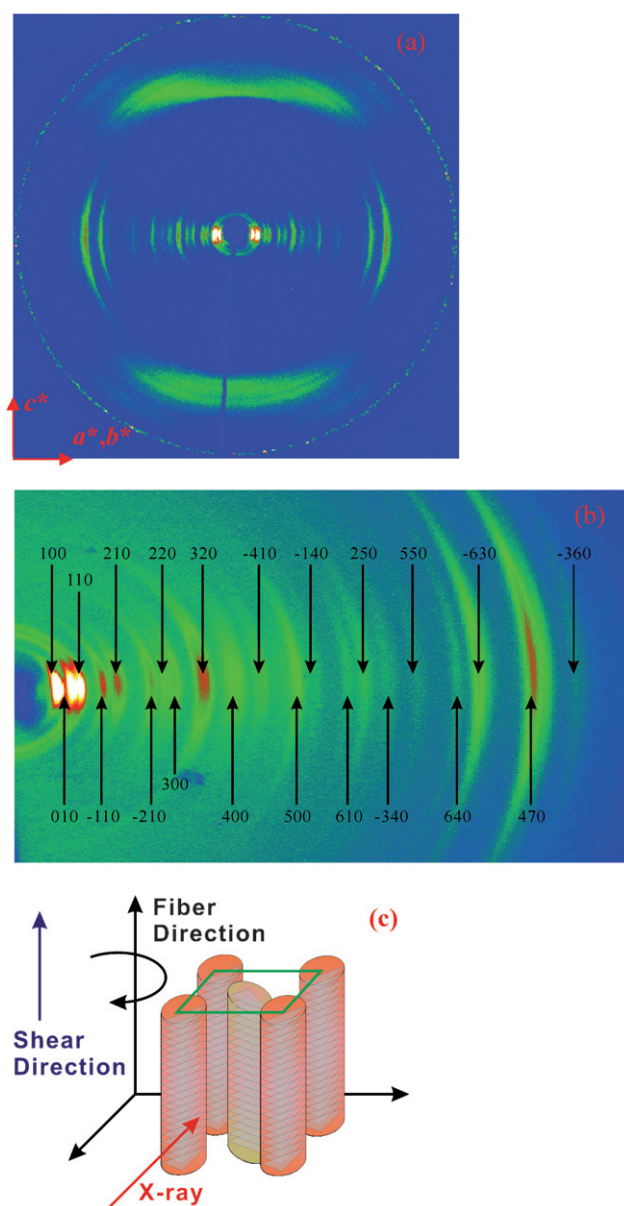


Fig. 16 2D WAXD pattern of HDATAN-[OC₁₄H₂₉]₆ at room temperature after the sample was mechanically sheared at 95 °C (a) and an enlarged 2D WAXD pattern along the equator (b). The shear and X-ray beam directions are shown in scheme (c).

Table 4 Crystallographic parameters of the crystalline phase at room temperature in HDATAN-[OC₁₄H₂₉]₆

(hkl) plane	2 θ /deg		<i>d</i> -Spacing/nm	
	Expt. ^a	Calcd. ^b	Expt. ^a	Calcd. ^b
100	2.33	2.33	3.79	3.79
010	2.93	2.93	3.02	3.02
110	3.24	3.25	2.73	2.72
$\bar{1}10$	4.17	4.18	2.12	2.12
210	4.75	4.83	1.86	1.83
$\bar{2}10$	6.08	6.10	1.45	1.45
220	6.62	6.49	1.34	1.36
300	6.97	6.99	1.27	1.26
320	8.01	7.90	1.10	1.12
400	9.47	9.33	0.93	0.95
410	10.41	10.46	0.85	0.85
500	11.70	11.66	0.76	0.76
$\bar{1}40$	12.45	12.52	0.71	0.71
610	13.64	13.56	0.65	0.65
250	14.27	14.22	0.62	0.62
340	15.16	15.12	0.58	0.59
550	16.29	16.28	0.54	0.54
460	17.68	17.74	0.50	0.50
630	18.42	18.37	0.48	0.48
001	19.25	19.24	0.46	0.46
121	20.06	20.09	0.44	0.44
470	20.35	20.34	0.44	0.44
360	20.73	20.59	0.43	0.43
221	21.01	21.01	0.42	0.42
331	21.66	21.61	0.41	0.41
341	22.69	22.76	0.39	0.39
650	22.70	22.80	0.39	0.39
651	26.08	26.16	0.34	0.34

^a Experimentally observed in Fig. 16. ^b Calculated based on the monoclinic unit cell of $a = 3.92$ nm, $b = 3.12$ nm, $c = 0.46$ nm, $\alpha = \beta = 90^\circ$, $\gamma = 75.3^\circ$.

the meridian. It is evident that this phase is a Col_r phase with $C2/m$ symmetry with dimensions of $a = 6.47$ and $b = 2.09$ nm. The molecules are stacked along the column direction having a d -spacing of 0.60 nm. Fig. 15c shows the molecular packing model of both phases.

For the series of compounds of HDATAN-[OR]₆, the symmetry of the rigid core becomes three-fold.^{60–62} Fig. 16a shows a 2D WAXD pattern for HDATAN-[OC₁₄H₂₉]₆ taken at room temperature after mechanical shearing at 95 °C. This pattern is also different from the 2D WAXD pattern reported in Fig. 13a; both a^* and b^* axes are along the equator. In detail, partially overlapped arcs on the equator in the low-angle region are attributed to three diffraction arcs at $2\theta = 2.33^\circ$, 2.93° and 3.24° (corresponding to d -spacings of 3.79, 3.02, and 2.73 nm), and they are assigned as the (100), (010) and (110) diffractions, respectively. There are also a series of relatively weak diffractions on the equator as shown in Fig. 16b. Weak and relatively diffuse diffractions can also be found on the meridian and in the quadrants. On the meridian, a relatively weak diffraction arc on the first layer was assigned as the (001) diffraction, and its d -spacing is 0.46 nm. The crystal structure was determined to be monoclinic. The calculated unit cell parameters are $a = 3.92$ nm, $b = 3.12$ nm, $c = 0.46$ nm, $\alpha = \beta = 90^\circ$, and $\gamma = 75.3^\circ$. The π – π interaction direction is still tilted from the normal direction of the columns but less so than the previous samples. The indices, the measured and calculated 2θ angles, and the d -spacing values are

listed in Table 4. All the relatively weak diffractions on the equator can be assigned based on these structural parameters as shown in Fig. 16b. The calculated density is 1.10 g cm^{−3} if two molecules are in one unit cell. This is consistent with the measured density of 1.09 g cm^{−3}. Fig. 16c shows the molecular packing model of the crystalline phase.

Conclusion

In summary, three new series of potentially useful photovoltaic materials with alkyl chains attached to a discotic fused rigid ring have been synthesized. DSC, WAXD and PLM techniques were used to investigate the side chain and molecular shape effect on phase behavior. The isotropization temperature decreases dramatically as the number of carbons in the flexible tails increases from 9 to 16 for the series of TQPP-[*t*-Bu]₂-[OR]₄. Using TQPP-[*t*-Bu]₂-[OC₁₀H₂₁]₄ as an example, at temperatures lower than 214.3 °C, two crystalline phases have been detected. The room temperature phase has been identified to be orthorhombic with dimensions of $a = 4.08$ nm, $b = 1.39$ nm, $c = 0.62$ nm, and $\alpha = \gamma = \beta = 90^\circ$. When the temperature is higher than 214.3 °C, a high-order Col_r phase with $C2/m$ symmetry has been detected. According to previous studies, no LC phases have been detected without modifying the 2 and 11 positions on the TQPP rigid core. The formation of an LC phase of TQPP-[*t*-Bu]₂-[OR]₄ indicates that the introduction of bulky *tert*-butyl group at the 2 and 11 positions on the TQPP core plays a key role in forming the LC phase.

Further modifying the linear flexible tails to branched alkyl chains led to TQPP-[*t*-Bu]₂-[OC₂₀H₄₁B]₄. The isotropization temperature of this material decreases significantly compared with similar linear tail lengths in TQPP-[*t*-Bu]₂-[OC₁₆H₃₃]₄. Only two LC phases formed below the temperature for the isotropic liquid phase. Even at room temperature, a high-order LC phase can be formed for this compound. The high-temperature phase was also identified as the Col_r phase with $C2/m$ symmetry. It is evident that the branched alkyl chains in the tails inhibit the formation of the crystalline phase when compared to the phase behaviors of TQPP-[*t*-Bu]₂-[OR]₄.

Extending the rigid core of TQPP to TPPQPP results in higher isotropization temperatures and a high-order columnar phase at room temperature for TPPQPP-[*t*-Bu]₂-[OC₂₀H₄₁B]₄ due to the relatively higher ratio of the rigid cores. The analysis of the phase structure of TQPP and TPPQPP with the same side chains revealed that the long axis of the rigid core is along the a -axis, and the core stacking is along the c -axis.

By modifying the symmetry of the rigid core to three-fold in the HDATAN-[OR]₆ series, a crystalline phase can be observed in the low-temperature region. Using HDATAN-[OC₁₄H₂₉]₆ as an example, this crystalline phase possesses a monoclinic unit cell with dimensions of $a = 3.92$ nm, $b = 3.12$ nm, $c = 0.46$ nm, $\alpha = \beta = 90^\circ$, and $\gamma = 75.3^\circ$.

Overall, by modifying the fused rigid ring size and shape as well as the location, lengths, and chemical structures of their flexible tails, we were able to control the phase behavior of model phenazine-based compounds which are important for photovoltaic applications. Among these factors, designing the non-crystalline alkyl tails is most effective to introduce the columnar LC phase into these types of materials.

Acknowledgements

The authors acknowledge that this work has been supported by the National Science Foundation (DMR-0516602 and DMR-0906898) and the Collaborative Center for Polymer Photonics, AFOSR. We also acknowledge the Perkin-Elmer Co. for providing the Diamond DSC instrument for our laboratory. B. R. K. acknowledges the support of the American Chemical Society Petroleum Research Fund (47343-B10) for the work at the American University of Beirut.

References

- 1 F. Garnier, R. Hajlaoui, A. Yassar and P. Srivastava, *Science*, 1994, **265**, 1864–1866.
- 2 C. D. Dimitrakopoulos, S. Purushothaman, J. Kymissis, A. Callegari and J. M. Shaw, *Science*, 1999, **283**, 822–824.
- 3 C. W. Tang and S. A. VanSlyke, *Appl. Phys. Lett.*, 1987, **51**, 913–915.
- 4 Y. Shirota and H. Kageyama, *Chem. Rev.*, 2007, **107**, 953–1010.
- 5 C. W. Tang, *Appl. Phys. Lett.*, 1986, **48**, 183–185.
- 6 L. Schmidt-Mende, A. Fechtenkötter, K. Mullen, E. Moons, R. H. Friend and J. D. MacKenzie, *Science*, 2001, **293**, 1119–1122.
- 7 J. Tant, Y. H. Geerts, M. Lehmann, V. De Cupere, G. Zucchi, B. W. Laursen, T. Bjørnholm, V. Lemaure, V. Marcq, A. Burquel, E. Hennebicq, F. Gardebien, P. Viville, D. Beljonne, R. Lazzaroni and J. Cornil, *J. Phys. Chem. B*, 2005, **109**, 20315–20323.
- 8 V. De Cupere, J. Tant, P. Viville, R. Lazzaroni, W. Osikowicz, W. R. Salaneck and Y. H. Geerts, *Langmuir*, 2006, **22**, 7798–7806.
- 9 A. J. J. M. Van Breemen, P. T. Herwig, C. H. T. Chlon, J. Sweelssen, H. F. M. Schoo, S. Setayesh, W. M. Hardeman, C. A. Martin, D. M. De Leeuw, J. J. P. Valetton, C. W. M. Bastiaansen, D. J. Broer, A. R. Popa-Merticaru and S. C. J. Meskers, *J. Am. Chem. Soc.*, 2006, **128**, 2336–2345.
- 10 S. Zimmermann, J. H. Wendorff and C. Weder, *Chem. Mater.*, 2002, **14**, 2218–2223.
- 11 O. Bunk, M. M. Nielsen, T. I. Solling, A. M. Van de Craats and N. Stutzmann, *J. Am. Chem. Soc.*, 2003, **125**, 2252–2258.
- 12 A. Tracz, J. K. Jeszka, M. D. Watson, W. Pisula, K. Müllen and T. Pakula, *J. Am. Chem. Soc.*, 2003, **125**, 1682–1683.
- 13 H. Monobe, K. Awazu and Y. Shimizu, *Adv. Mater.*, 2000, **12**, 1495–1499.
- 14 E. F. Gramsbergen, H. J. Hoving, W. H. De Jeu, K. Praefcke and B. Kohne, *Liq. Cryst.*, 1986, **1**, 397–400.
- 15 J. F. Van der Pol, E. Neeleman, J. W. Zwicker, R. J. M. Nolte, W. Drenth, J. Aerts, R. Visser and S. J. Picken, *Liq. Cryst.*, 1989, **6**, 577–592.
- 16 P. Herwig, C. W. Kayser, K. Müllen and H. W. Spiess, *Adv. Mater.*, 1996, **8**, 510–513.
- 17 N. B. McKeown, *Phthalocyanine Materials: Structure, Synthesis and Function*, Cambridge University Press, Cambridge, 1998.
- 18 D. Markovitsi, S. Marguet, J. Bondkowski and S. Kumar, *J. Phys. Chem. B*, 2001, **105**, 1299–1306.
- 19 A. M. van de Craats and J. M. Warman, *Adv. Mater.*, 2001, **13**, 130–133.
- 20 R. I. Gearba, M. Lehmann, J. Levin, D. A. Ivanov, M. H. J. Koch, J. Barbera, M. G. Debije, J. Piris and Y. H. Geerts, *Adv. Mater.*, 2003, **15**, 1614–1618.
- 21 M. Lehmann, G. Kestemont, R. G. Aspe, C. Buess-Herman, M. H. J. Koch, M. G. Debije, J. Piris, M. P. de Haas, J. M. Warman, M. D. Watson, V. Lemaure, J. Cornil, Y. H. Geerts, R. Gearba and D. A. Ivanov, *Chem.–Eur. J.*, 2005, **11**, 3349–3362.
- 22 S. Leng, B. Wex, L. H. Chan, M. J. Graham, S. Jin, A. J. Jing, K.-U. Jeong, R. M. Van Horn, B. Sun, M. Zhu, B. R. Kaafarani and S. Z. D. Cheng, *J. Phys. Chem. B*, 2009, **113**, 5403–5411.
- 23 J. Hu, D. Zhang, S. Jin, S. Z. D. Cheng and F. W. Harris, *Chem. Mater.*, 2004, **16**, 4912–4915.
- 24 J. Hu, PhD dissertation, University of Akron, Akron, OH, USA, 2005.
- 25 S. Z. D. Cheng, Z. Wu, M. Eashoo, S. L. Hsu and F. W. Harris, *Polymer*, 1991, **32**, 1803–1810.
- 26 M. Eashoo, Z. Wu, A. Zhang, D. Shen, C. Tse, F. W. Harris, S. Z. D. Cheng, K. H. Gardner and B. S. Hsiao, *Macromol. Chem. Phys.*, 1994, **195**, 2207–2225.
- 27 J. J. Ge, A. Zhang, K. W. McCreight, R.-M. Ho, S.-Y. Wang, X. Jin, F. W. Harris and S. Z. D. Cheng, *Macromolecules*, 1997, **30**, 6498–6506.
- 28 A. Kellera and S. Z. D. Cheng, *Polymer*, 1998, **39**, 4461–4487.
- 29 S. Z. D. Cheng and A. Keller, *Annu. Rev. Mater. Sci.*, 1998, **28**, 533–562.
- 30 S. Z. D. Cheng, *Phase Transitions in Polymers: the Role of Metastable States*, Elsevier, Amsterdam, 2008.
- 31 G. Ungar, J. L. Feijoo, V. Percec and R. Yourd, *Macromolecules*, 1991, **24**, 953–957.
- 32 M. A. Yandrasits, S. Z. D. Cheng, A. Zhang, J. Cheng, B. Wunderlich and V. Percec, *Macromolecules*, 1992, **25**, 2112–2121.
- 33 R. Pardey, A. Zhang, P. A. Gabori, F. W. Harris, S. Z. D. Cheng, J. Adduci, J. V. Facinelli and R. W. Lenz, *Macromolecules*, 1992, **25**, 5060–5068.
- 34 R. Pardey, S. S. Wu, J. Chen, F. W. Harris, S. Z. D. Cheng, A. Keller, J. Adduci, J. V. Facinelli and R. W. Lenz, *Macromolecules*, 1994, **27**, 5794–5802.
- 35 Y. Yoon, A. Zhang, R.-M. Ho, S. Z. D. Cheng, V. Percec and P. Chu, *Macromolecules*, 1996, **29**, 294–305.
- 36 Y. Yoon, R.-M. Ho, B. Moon, D. Kim, K. W. McCreight, F. Li, F. W. Harris, S. Z. D. Cheng, V. Percec and P. Chu, *Macromolecules*, 1996, **29**, 3421–3431.
- 37 R.-Q. Zheng, E.-Q. Chen, S. Z. D. Cheng, F. Xie, D. Yan, T. He, V. Percec, P. Chu and G. Ungar, *Macromolecules*, 1999, **32**, 3574–3582.
- 38 R.-Q. Zheng, E.-Q. Chen, S. Z. D. Cheng, F. Xie, D. Yan, T. He, V. Percec, P. Chu and G. Ungar, *Macromolecules*, 1999, **32**, 6981–6988.
- 39 A. J. Jing, O. Taikun, C. Y. Li, F. W. Harris and S. Z. D. Cheng, *Polymer*, 2002, **43**, 3431–3440.
- 40 S. Jin, Y. Ma, S. C. Zimmerman and S. Z. D. Cheng, *Chem. Mater.*, 2004, **16**, 2975–2977.
- 41 H. Shen, K.-U. Jeong, M. Graham, S. Leng, H. Huang, B. Lotz, H. Hou, F. Harris and S. Cheng, *J. Macromol. Sci. Phys.*, 2006, **45**, 215–229.
- 42 H. Shen, K.-U. Jeong, H. Xiong, M. J. Graham, S. Leng, J. X. Zheng, H. Huang, M. Guo, F. W. Harris and S. Z. D. Cheng, *Soft Matter*, 2006, **2**, 232–242.
- 43 K.-U. Jeong, S. Jin, J. J. Ge, B. S. Knapp, M. J. Graham, J. Ruan, M. Guo, H. Xiong, F. W. Harris and S. Z. D. Cheng, *Chem. Mater.*, 2005, **17**, 2852–2865.
- 44 K.-U. Jeong, B. S. Knapp, J. J. Ge, M. J. Graham, Y. Tu, S. Leng, H. Xiong, F. W. Harris and S. Z. D. Cheng, *Polymer*, 2006, **47**, 3351–3362.
- 45 Y. Xu, S. Leng, C. Xue, R. Sun, J. Pan, J. Ford and S. Jin, *Angew. Chem., Int. Ed.*, 2007, **46**, 3896–3899.
- 46 M.-S. Hsiao, J. X. Zheng, S. Leng, R. M. Van Horn, R. P. Quirk, E. L. Thomas, H.-L. Chen, B. S. Hsiao, L. Rong, B. Lotz and S. Z. D. Cheng, *Macromolecules*, 2008, **41**, 8114–8123.
- 47 B. Y. Tang, J. J. Ge, A. Zhang, B. Calhoun, P. Chu, H. Wang, Z. Shen, F. W. Harris and S. Z. D. Cheng, *Chem. Mater.*, 2001, **13**, 78–86.
- 48 B. Y. Tang, A. J. Jing, C. Y. Li, Z. Shen, H. Wang, F. W. Harris and S. Z. D. Cheng, *Cryst. Growth Des.*, 2003, **3**, 375–382.
- 49 H. W. Neuling, H. Stegemeyer, K. Praefcke and B. Kohne, *Z. Naturforsch., A: Phys. Sci.*, 1987, **42**, 631–635.
- 50 S. Laschat, A. Baro, N. Steinke, F. Giesselmann, C. Haegeler, G. Scalia, R. Judele, E. Kapatsina, S. Sauer, A. Schreivogel and M. Tosoni, *Angew. Chem., Int. Ed.*, 2007, **46**, 4832–4887.
- 51 F. C. Frank and S. Chandrasekhar, *J. Phys. (Les Ulis, Fr.)*, 1980, **41**, 1285–1288.
- 52 J. Billard, J. C. Dubois, C. Vaucher and A. M. Levelut, *Mol. Cryst. Liq. Cryst.*, 1981, **66**, 435–442.
- 53 A. M. Levelut, *J. Chim. Phys. Phys.-Chim. Biol.*, 1983, **80**, 149–161.
- 54 C. Destrade, P. Foucher, H. Gasparoux, T. Nguyen Huu, A. M. Levelut and J. Malthete, *Mol. Cryst. Liq. Cryst.*, 1984, **106**, 121–146.
- 55 B. Gluesen, W. Heitz, A. Kettner and J. H. Wendorff, *Liq. Cryst.*, 1996, **20**, 627–633.
- 56 F. Morale, R. W. Date, D. Guillon, D. W. Bruce, R. L. Finn, C. Wilson, A. J. Blake, M. Schroeder and B. Donnio, *Chem.–Eur. J.*, 2003, **9**, 2484–2501.
- 57 S. K. Prasad, D. S. S. Rao, S. Chandrasekhar and S. Kumar, *Mol. Cryst. Liq. Cryst.*, 2003, **396**, 121–139.

-
- 58 B. Donnio, B. Heinrich, H. Allouchi, J. Kain, S. Diele, D. Guillon and D. W. Bruce, *J. Am. Chem. Soc.*, 2004, **126**, 15258–15268.
- 59 *International Tables for X-ray Crystallography, Vol. II: Mathematical Tables*, ed. J. S. Kasper, K. Lonsdale, Kynoch Press for the International Union of Crystallography, Birmingham, 1959.
- 60 L. Y. Chiang, C. R. Safinya, N. A. Clark, K. S. Liang and A. N. Bloch, *J. Chem. Soc., Chem. Commun.*, 1985, 695–696.
- 61 M. Kastler, J. Schmidt, W. Pisula, D. Sebastiani and K. Mullen, *J. Am. Chem. Soc.*, 2006, **128**, 9526–9534.
- 62 J. J. van Gorp, J. A. J. M. Vekemans and E. W. Meijer, *Mol. Cryst. Liq. Cryst.*, 2003, **397**, 491–505.